High-Cycle Tensile-Tensile Fatigue Performance of Niobium Alloy: Conventional vs Wire-Arc Additive Manufacturing

Gazi Tanvir, Md Abdul Karim, Namjung Kim, Yongho Jeon, Duck Bong Kim

PII: S2238-7854(24)03057-6

DOI: https://doi.org/10.1016/j.jmrt.2024.12.254

Reference: JMRTEC 12689

To appear in: *Journal of Materials Research and Technology*

Received Date: 31 August 2024

Revised Date: 29 December 2024

Accepted Date: 29 December 2024

Please cite this article as: Tanvir G, Karim MA, Kim N, Jeon Y, Kim DB, High-Cycle Tensile-Tensile Fatigue Performance of Niobium Alloy: Conventional vs Wire-Arc Additive Manufacturing, *Journal of Materials Research and Technology*, https://doi.org/10.1016/j.jmrt.2024.12.254.

High-Cycle Tensile-Tensile Fatigue Performance of Niobium Alloy: Conventional vs Wire-Arc Additive Manufacturing

Gazi Tanvir[a], Md Abdul Karim[a], Namjung Kim[b], Yongho Jeon[c**], and Duck Bong Kim[d]*

[a] Department of Mechanical Engineering, Tennessee Technological University, Cookeville, TN 38505, United States

[b] Department of Mechanical Engineering, Gachon University, Seongnam, 13120, South Korea

[c] Department of Mechanical Engineering, Ajou University, Suwon, Gyeonggi-do, Korea

[d] Department of Manufacturing and Engineering Technology, Tennessee Technological University, Cookeville, TN 38505, United States

**Co-corresponding author. Email address: princaps@ajou.ac.kr
*Corresponding author. E-mail address: dkim@tntech.edu (D.B. Kim).

Abstract

This study explores the high-cycle fatigue (HCF) behavior of a niobium alloy, NbZr1, fabricated using wire-arc additive manufacturing (WAAM), and compares its fatigue strength to that of its powder metallurgy (PM)-produced counterpart. The analysis was conducted at three different stress levels, each characterized by a non-zero mean stress and a stress ratio of 0.1. The fatigue life ranged from 10^4 to 10^8 cycles under tensile-tensile fatigue loading for all tested samples. WAAM-produced NbZr1 exhibited a shorter average fatigue life compared to PM-NbZr1. Examination of the fracture surfaces revealed consistent fracture morphology across all loading conditions in PM-NbZr1 samples, whereas WAAM-NbZr1 samples showed varied fracture behavior. Notably, the crack propagation regions in WAAM-NbZr1 exhibited contrasting behaviors under different loading conditions. While PM-NbZr1 demonstrated typical ductile failure with elongated dimples near the final fracture region, WAAM-NbZr1 showed more pronounced cleavage crack growth, accompanied by void nucleation and coalescence along the ZrO_2 particles during fatigue crack propagation. The interdendritic regions containing fine ZrO_2 particles were identified as key factors influencing crack propagation and final fracture location in WAAM-NbZr1.

Keywords:

High-cycle fatigue, Wire-arc additive manufacturing, Powder metallurgy, Refractory alloy, Niobium

1. Introduction:

Refractory metals are highly valued for their exceptional resistance to heat and wear, making them indispensable for high-temperature and high-stress applications. Among these metals, niobium (Nb) alloys are particularly noteworthy due to their excellent combination of strength and superconducting capabilities. NbZr1, in particular, stands out within the spectrum of Nb-alloys due to its remarkable corrosion resistance in various aqueous environments and low sensitivity to thermal neutrons [1]. This alloy is crucial for structural components in high-temperature reactor cores, hypersonic missiles, and jet engine turbine blades. Given the cyclic stresses caused by missile skin vibrations, turbine blade vibrations, and fluid flow in nuclear reactor cores, understanding the fatigue behavior of NbZr1 is essential. Its high-cycle fatigue strength is especially important for enhancing service life and minimizing the need for part replacements.

Several previous studies endeavored to reveal the fatigue properties of the NbZr1 alloy. A previous study investigated the reverse bending fatigue behavior of NbZr1 produced by electron beam melting and cold rolling [2]. In this study, fatigue loading was controlled based on total displacement, and stresses were estimated accordingly. The results indicated that the recrystallized NbZr1 alloy did not exhibit an endurance limit within the tested range. In the high-cycle fatigue region, around 10^7 cycles, the alloy withstood a maximum stress exceeding 185 MPa. They also compared their findings with Begley et al. [3], who studied annealed pure Nb sheet produced by powder metallurgy (PM). The pure Nb showed a lower fatigue strength than the recrystallized NbZr1 alloy as the cold-rolled Nb demonstrated increased strength over annealed parts at a similar number of cycles. Increased metallurgical bond induced by the arc melting produced higher strength of the alloy compared to the PM process as indicated by their findings. Recently, Rubitschek et al. investigated the fatigue performance of Nb-2%Zr for biocompatible body fluid applications [4]. This study inspected both low-cycle and high-cycle fatigue regions for Nb-2%Zr produced by equal channel angular processing (ECAP). They reported that the ultra-fine grain alloy endured around 2×10^6 cycles with a mean fatigue limit of 291 MPa, demonstrating superior fatigue performance over conventional grain size conditions, primarily due to its higher monotonic strength.

Compared to traditional manufacturing methods, recent advancements in additive manufacturing (AM) offer a cost-efficient alternative with benefits such as reduced material waste, capability to swiftly produce intricate designs, and decreased inventory expenses [5]. In particular, wire-arc additive manufacturing (WAAM) techniques enable the manufacturing of complex shapes at high deposition rates, require minimal setup costs, utilize a wide range of wire materials, and facilitate the production of large-scale metal structures [6]. The use of NbZr1 in the WAAM process has shown potential for high-temperature applications, with tensile properties in the as-built state comparable to those achieved through conventional fabrication methods. Islam et. al examined the microstructural evolution and tensile characteristics of NbZr1 produced via the tungsten inert gas (TIG)-based WAAM process, revealing that the yield strength (YS), ultimate tensile strength (UTS), and elongation were comparable to those from traditional processes [7].

Despite the numerous benefits of WAAM over traditional processes, it includes several undesirable features, such as inclusions and residual thermal stress, due to the non-equilibrium thermal cycles experienced by the parts [8]. These issues can adversely affect the fatigue properties of NbZr1 [9]. Additionally, the solidification process in AM parts differs significantly from that of conventionally produced parts, resulting in considerable variations in microstructural features. For instance, directional solidification resulting in columnar grain structures and elemental micro-segregation can negatively impact the high-cycle fatigue performance of WAAM-produced NbZr1. Notwithstanding these factors, the fatigue performance of NbZr1 produced using this manufacturing process has not yet been fully assessed. As AM techniques offer obvious benefits over traditional processes, it is crucial to investigate the fatigue properties of WAAM-produced NbZr1 structures for their further development and subsequent applications. Nevertheless, the lack of a WAAM-specific material structure-property database for NbZr1 remains a significant barrier to its use in fatigue-critical applications.

This study aims to evaluate the fatigue behavior of the NbZr1 alloy fabricated using the WAAM process, with a particular emphasis on its high-cycle tensile-tensile fatigue properties at three distinct stress levels. The performance of WAAM-produced NbZr1 is compared to its counterpart made via powder metallurgy. Special attention is given to elucidating the significance of the WAAM-induced microstructure on the fatigue performance of NbZr1 in the high-cycle fatigue regime.

2. Experimental procedures

2.1. Materials and processing methods

NbZr1 alloy samples used in this study were sourced from two different manufacturing processes: PM and WAAM. The NbZr1 plate, produced via PM followed by cold rolling (conforming to ASTM B393-09), was supplied by ALB Materials Inc. and served as the conventionally manufactured sample. For the WAAM samples, NbZr1 wire was deposited onto NbZr1 substrates (100 mm × 25 mm × 5 mm) using a TIG-based WAAM setup with 200A of welding current. The details of the WAAM setup and the process parameters were documented in a previous study [7]. The chemical composition of the NbZr1 wire and plate (PM-sample) is provided in **Table 1**. A total of three thin walls were deposited, each with dimensions of 100 mm × 40 mm × 7 mm. During the thin wall deposition, an interpass temperature of 100 °C was maintained between each successive layer.

Table 1: Elemental composition (wt.%) of NbZr1 wire (WAAM-NbZr1) and NbZr1 plate (PM-NbZr1).

Alloying elements	Nb	Zr	Ta	O	W	Mo	Hf	C	N	Fe	Al	Si	Ni
NbZr1wire	Bal.	0.8-1.2	0.5	0.25	0.05	0.05	0.02	0.01	0.01	0.01	0.005	0.005	0.005
NbZr1 plate	Bal.	0.86	.04	.009	0.022	<10 ppm	<10 ppm	0.003	1 ppm	3 ppm	-	<1 ppm	1 ppm

2.2 Fatigue test

Fig. 1 depicts the schematic of the fatigue test setup, loading type, and sample dimensions. The samples were cut using wire electron discharge machining (EDM) from both the WAAM deposit and the NbZr1 plate into dog bone-shaped fatigue specimens, as shown in **Fig. 1**(c). The fatigue test samples were designed following the ASTM E466 standard. MTS 810 Material Test System – a 100kN high-rate uniaxial servo-hydraulic load frame – was used for the fatigue test. Given the small grip area of the samples relative to the machine grip, a customized specimen holder was designed for the top and bottom frames (**Fig. 1**(a)). A frequency of 20 Hz was utilized for the fatigue load, and the stress ratio was maintained at R = 0.1, for all the test pieces with mean stress on the tension side indicating a tensile-tensile fatigue test. All the samples were ground and polished with SiC abrasives (grit sizes of 240-1200) to maintain a roughness value of 0.3-0.4 μm. **Table 2** presents the test parameters used for three stress levels.

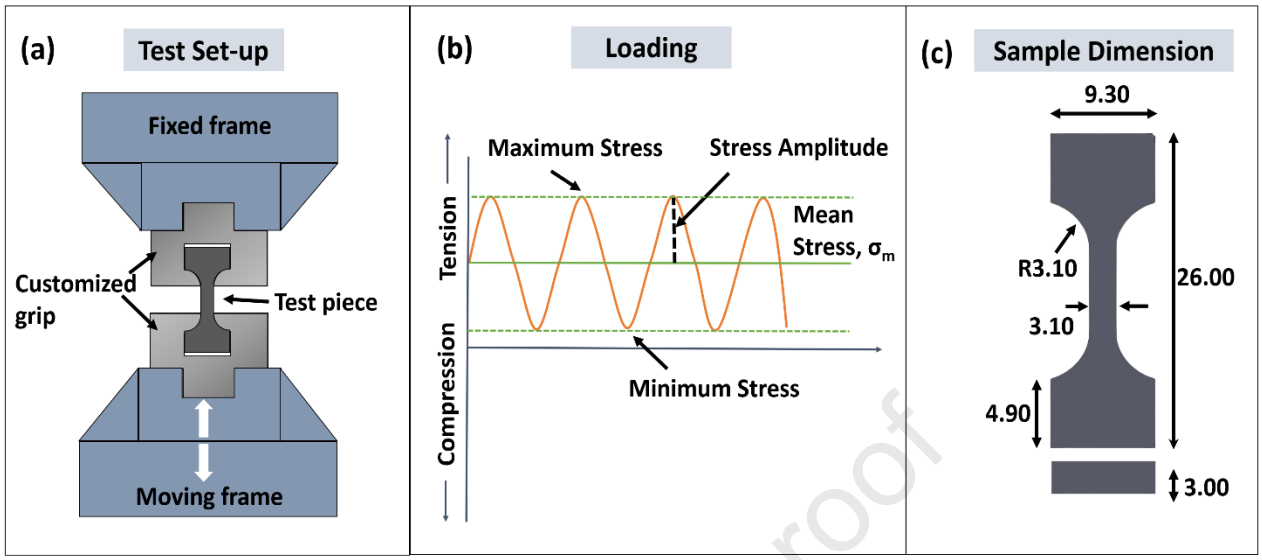

Figure 1: Schematic of (a) fatigue test setup, (b) fatigue load type, and (c) fatigue test sample, sample dimensions in mm.

Table 2: Fatigue loading conditions for PM and WAAM produced NbZr1.

Stress level	Maximum Stress (MPa)	Minimum Stress (MPa)	Mean Stress (MPa)	Stress Amplitude (MPa)	Stress Ratio	Frequency (Hz)
Level-1	250	25	137.5	112.5	0.1	20
Level-2	200	20	110	90	0.1	20
Level-3	150	15	82.5	67.5	0.1	20

2.3 Material characterization

The characterization of the PM and WAAM specimens involved precise transverse sectioning using wire-EDM. The sectioned specimens were then mounted in Bakelite thermosetting powder. Metallographic preparation followed, using grinding wheels with SiC abrasives of various grits (240, 400, 600, 800, and 1200) and diamond paste solutions with particle sizes of 3 and 1 µm. A specially prepared etchant [10mL HF + 10mL HNO_3 + 30mL lactic acid] was used for chemical etching. For microstructure, elemental analysis, and fracture surface analysis, a Hitachi SU 7000 scanning electron microscope (SEM) equipped with an Octane Elect Super energy-dispersive X-ray spectroscope (EDS) was employed. The tensile test was performed in the rolled direction for the PM part and in the build direction for the WAAM part using a uniaxial tensile testing system (Test Resources 810 E4 Electrodynamic Test Machine). The detailed tensile test procedure was reported in a previous study [7].

3. Results

3.1 Initial Microstructure

The initial microstructures of WAAM-NbZr1 and PM-NbZr1 are shown in **Fig.** 2(a-d). The WAAM process produced a coarse-grained structure with columnar dendrites aligned with the build direction. This alignment results in grain boundaries that are predominantly parallel to the applied stress, a characteristic of the WAAM process where directional solidification aligns with the build direction. The WAAM-NbZr1 microstructure consists of a Nb matrix with fine ZrO_2 precipitates distributed in the interdendritic regions.

In contrast, the PM-NbZr1 structure mainly comprises sintered NbZr1 particles with pores formed during sintering. These pores are mostly spherical, unevenly distributed, and measure less than 5µm (approx.) in diameter. Additionally, since the substrate NbZr1 underwent a cold rolling process, the PM-NbZr1 microstructure is oriented in the rolling direction (**Fig.** 2(c)).

Fig. 2(e) shows the XRD spectra for both NbZr1 samples, recorded from 20° to 90° with a step size of 0.02°. Major peaks were identified at 38.19°, 55.38°, 69.43°, and 82.02°, which corresponded to the BCC-Nb matrix in WAAM-NbZr1, consistent with a prior study [7]. Additionally, small peaks at 27.63° and 32.01° were identified indicating the existence of ZrO_2 within the microstructure. The PM-NbZr1 spectra showed prominent peaks identical to those of the WAAM-NbZr1 for Nb, but no ZrO_2 phase was detected. Therefore, the presence of ZrO_2 inclusions in the interdendritic regions of as-built WAAM-NbZr1 is the crucial distinction between the two samples which formed during the solidification of deposited material [7].

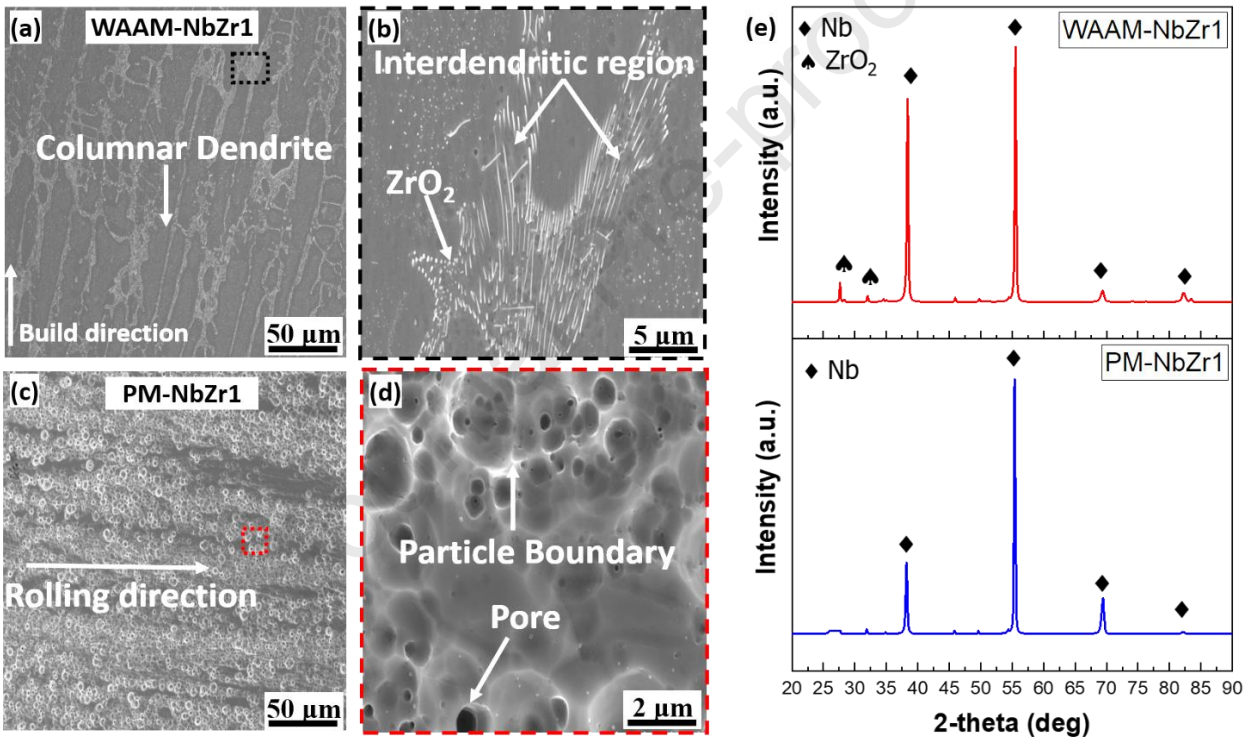

Figure 2: Microstructure of (a)-(b) PM-NbZr1 and (c)-(d) WAAM-NbZr1 before fatigue test, (e) XRD spectra of the two samples.

3.2 Monotonic properties

Fig. 3 displays the uniaxial tensile test results for WAAM and PM NbZr1 samples. The yield strength of the PM sample is found 325±3 MPa, whereas the WAAM sample exhibits a yield strength of 280±5 MPa (**Table 3**). This indicates that WAAM-NbZr1 has lower tensile strength compared to PM-NbZr1. However, both samples show similar elongation, suggesting comparable ductility. The difference in tensile strength can be attributed to significant microstructural variations between the samples. In WAAM-NbZr1, the columnar dendrites aligned with the build direction resulted in grain boundaries parallel to the applied stress. This alignment reduces the effectiveness of grain boundaries as barriers to dislocation movement,

leading to lower yield strength but similar ductility. Additionally, the presence of fine ZrO_2 particles in WAAM-NbZr1 may have adverse effect on its tensile strength. Although it is unclear how these precipitates would affect the uniaxial tensile property, they potentially increase the hardness of the material [7]. These precipitates could also significantly affect fatigue behavior under cyclic loading. On the other hand, the improved tensile strength in PM-NbZr1 is largely due to the enhanced metallurgical bonds achieved through sintering.

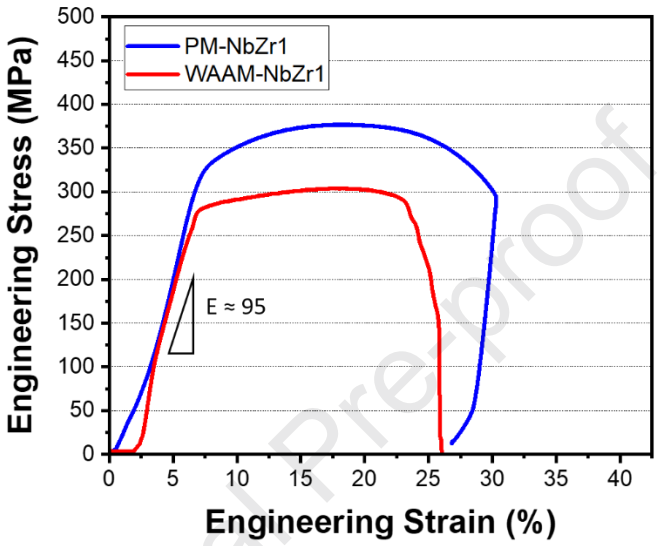

Figure 3: Stress-strain curves under uniaxial tensile test for WAAM-NbZr1 and PM-NbZr1.

Table 3: Uniaxial tensile properties of PM-NbZr1 and WAAM-NbZr1.

Sample	Yield stress (MPa)	Tensile stress (MPa)	Elongation (%)	Young's modulus (GPa)
PM-NbZr1	325±3	380±3	27±1	95±1
WAAM-NbZr1	280±5	310±5	26±2	95±1

3.3 High-cycle fatigue (HCF)

In HCF testing, where stress is predominantly controlled, it is critical to select a stress range that minimizes large plastic deformation [10]. Accordingly, based on the tensile test results, a maximum stress level below the yield strength of NbZr1 was chosen for fatigue loading. **Fig.** 3 shows the HCF test results of PM-NbZr1 and WAAM-NbZr1. Although the stress ratio was identical in all experiments, stress amplitude was varied, resulting in different fatigue responses at different stress levels. Increasing the stress amplitude resulted in reduced number of cycles to failure from 3.6×10^7 to 3.5×10^4. Most of the tested samples exhibited a fatigue life within the HCF region. Typically, HCF occurs between 10^4 and 10^7 cycles, while fatigue life below 10^4 cycles is considered low cycle fatigue, and life exceeding 10^7 cycles is classified as very high-cycle fatigue [11] [12]. Notably, a few samples demonstrated a very high fatigue life at stress level-3, which had the minimum stress amplitude.

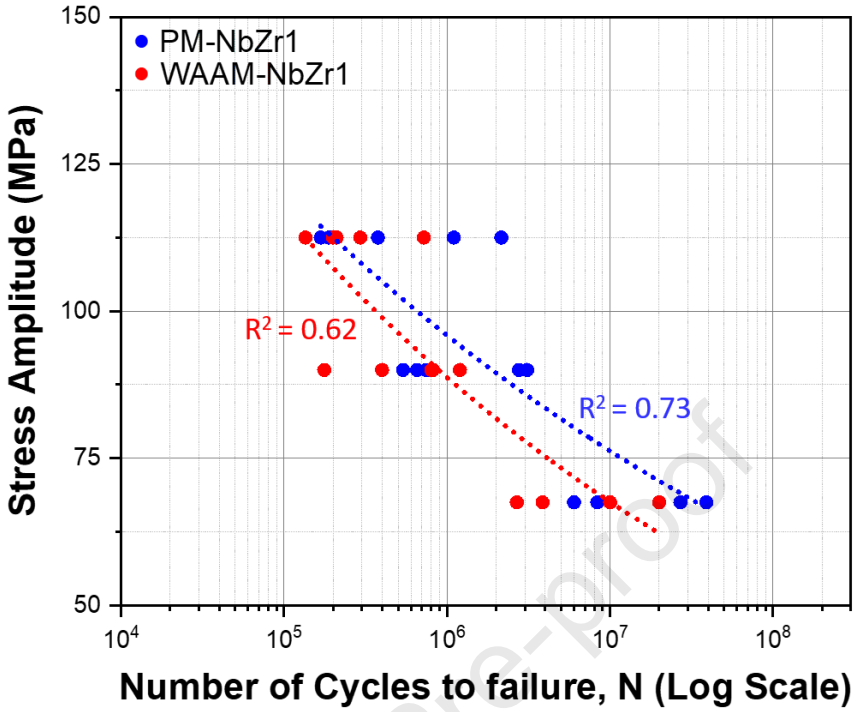

Figure 4: Tensile-tensile high-cycle fatigue test results for PM-NbZr1 and WAAM-NbZr1, with a dotted red and blue lines showing the non-linear curve fitting for WAAM and PM samples respectively.

A non-linear curve fitting, shown as red and blue dotted line in **Fig**. 3, indicates the increasing trend in fatigue life with decreasing stress amplitude for both NbZr1. This is typical of a fatigue test as increase in stress amplitude results in faster crack development leading towards final failure. From the test results it is evident that no endurance limit is present within the tested range for this alloy. However, due to the limited number of data points, the exact shape of the S-N plot could not be identified. Additionally, significant data scattering was observed across all stress levels, which is typical of fatigue tests. Source of scatter can include differences in the surface condition of tested samples and the indeterminant nature of actual maximum stress [2]. As both of the fatigue crack initiation site and the crack propagation region growth changes based on these conditions, it affects the overall fatigue life. However, reduced scattering in the S-N plot is seen for a lower number of cycles compared to a higher number of cycles. At high stress amplitudes, sharp stress concentrations develop on the sample, promoting crack formation on the surface and eventually leading to fatigue failure. At lower stress amplitudes, crack initiation can be influenced by surface defects and inclusions in the microstructure, such as ZrO_2 particles in the interdendritic region. At higher stress levels, crack initiation is less sensitive to these irregularities [13]. When comparing the two manufacturing processes, PM-NbZr1 exhibited increased resistance to failure at all stress levels compared to the WAAM sample, which can be attributed to its higher tensile strength. Moreover, the significant differences in the microstructure of these two samples played a crucial role in their differing fatigue responses.

In addition to the fatigue life, total axial strain was measured as shown in **Fig. 5**(a) demonstrating the evolution of strain in the sample throughout the entire cyclic loading. It is evident that most of the samples did not undergo any substantial strain during their fatigue lives until the final failure. Since high-cycle fatigue loading primarily imposes elastic strain, the total axial strain in these samples remained below 1% until the end of their fatigue lives. Notably, the stress levels had some effect on the total strain as with

increase in maximum stress, the strain accumulation increased for all sample. The PM-NbZr1 samples showed slightly more strain accumulation than the WAAM-NbZr1 which is in accordance with the ductility observed in the uniaxial tensile test shown in **Fig. 3**. **Fig. 5**(b) highlights the correlation of mean stress and total axial strain where increase in positive mean stress resulted in greater strain accumulation after fatigue fracture. Similar effect of positive mean stress on the cumulative strain was recorded by high-cycle fatigue experiments in a previous study [14]. In order to obtain further insight from these results, fracture surface analysis was conducted.

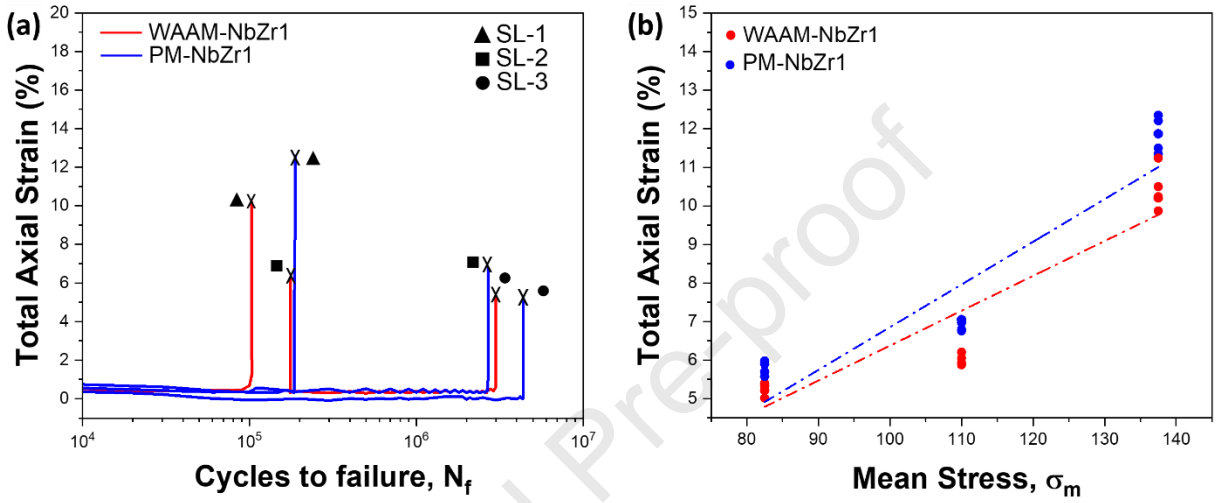

Figure 5: (a) Evaluation of total axial strain during cyclic loading for three different stress levels (SL) of WAAM and PM NbZr1, (b) Change in total axial strain for different mean stress.

3.4 Fracture surface

Fig. 6 highlights the characteristic fracture surfaces of PM-NbZr1 and WAAM-NbZr1 across all stress levels. It is evident that all PM-NbZr1 samples exhibited similar fracture morphology with the presence of shear lips. In contrast, WAAM-NbZr1 samples displayed significantly different fracture characteristics under various loading conditions. When comparing crack initiation, WAAM-NbZr1 samples had a higher number of initiation sites at lower peak stress levels than PM-NbZr1. Additionally, unlike PM-NbZr1, crack initiation sites for WAAM-NbZr1 were distributed around the entire perimeter of the sample. The presence of residual stresses could be a reason for these multiple crack initiation sites for WAAM-NbZr1. During the non-equilibrium cooling cycle of WAAM process, significant stresses are induced between the deposited layers. Formation of residual stress is associated with changes in material properties, such as surface topography or local strain hardening effects, which substantially impact crack formation [15].

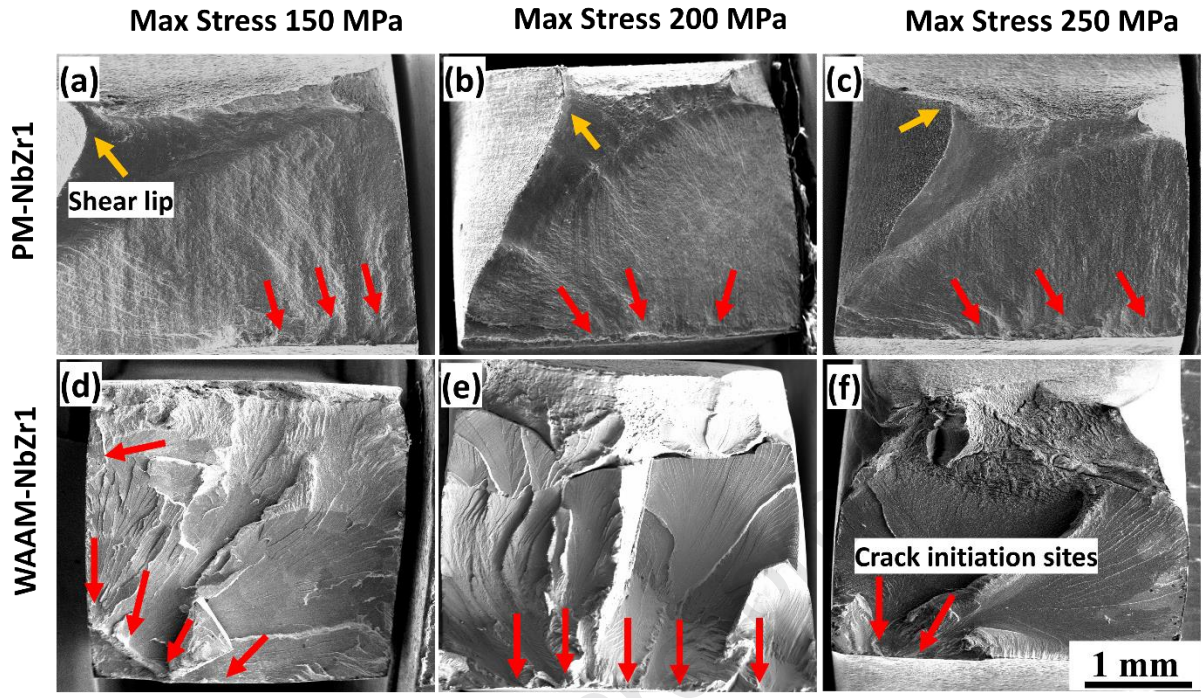

Figure 6: At three different stress levels, fracture surface of PM-NbZr1 (a-c) and WAAM-NbZr1 (d-f).

Fig. 7 presents the SEM images of the fracture surface of PM-NbZr1 and WAAM-NbZr1 samples subjected to stress level-1. The images reveal typical axial fatigue fracture characteristics, including the fatigue crack propagation zone, final fracture zone, and a distinct shear lip, which is particularly evident in the PM-NbZr1 sample. The shear lips extend around the final fracture area, indicating the location of failure. Besides, the presence of elongated dimples is visible near the final failure zone, as seen in **Fig.** 7(d). This indicates a substantial amount of plastic deformation occurred through localized shear before the final separation of the sample [16]. In contrast, the WAAM-NbZr1 sample had a rougher appearance at the final fracture zone with less pronounced shear lips. All tested samples exhibit multiple crack initiation sites, as indicated by the ratchet marks in **Figs.** 7(b) and 7(f).

For both sample types, cracks originated from the surface, likely due to surface irregularities such as notches or scratches. Compared to the PM samples, the WAAM samples showed a greater number of ratchet marks in the crack initiation region, extending towards the crack propagation region, highlighting a notable difference between the two sample. As the crack grew and reached a critical size where the remaining cross-section could no longer support the load, a sudden fracture of the specimen occurred. Interestingly, although PM-NbZr1 had porosities in its initial microstructure, the influence of these porosities could not be identified from the crack initiation sites. This might be due to the size and distribution of the pores in the PM microstructure, as larger pores usually have a more significant influence on fatigue crack initiation. The correlation between the size of a pore and the maximum stress intensity factor was reported in a previous study for mode I (tensile-opening) loading, where an increase in cross-sectional area of the pore increased the maximum stress intensity factor [17]. However, in the present study, most of the pores were very fine, with an average pore diameter of less than 5µm, which could be insignificant to influence fatigue crack initiation [18].

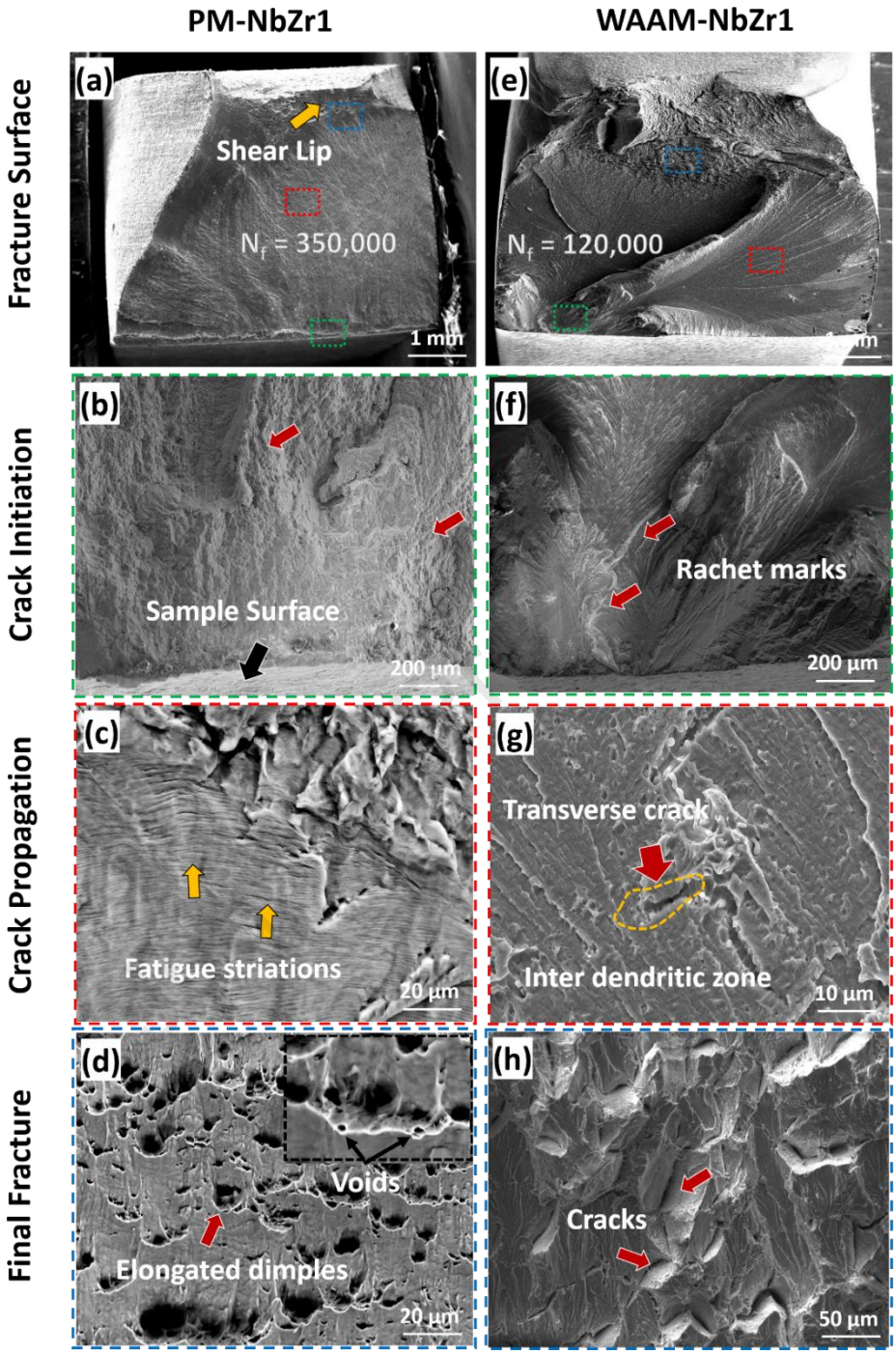

Figure 7:(a) Fracture surface of PM-NbZr1, (b)-(d) enlarged view from the green, red, and blue areas in (a). (e) Fracture surface of WAAM-NbZr1, (f)-(h) enlarged view from (e).

In the crack propagation region, fatigue striation marks are visible for PM parts (**Fig.** 7(c)), whereas in the WAAM sample, fatigue striation marks are less noticeable. Crack propagation is highly localized at the interdendritic zone (**Fig.** 7(g)) for WAAM samples. Transverse cracks have formed along with longitudinal cracks in the direction perpendicular to the applied cyclic stress in both of them. As a result of the overall fracture development process, the fatigue crack propagation zones are comparatively smoother than the

final fracture zones for both samples. However, the crack propagation zone of the WAAM part is comparatively rougher than that of PM-NbZr1, mainly due to the presence of oxide inclusions in the microstructure. Oxide particles generally obstruct the main crack growth paths and deviate them to different non-coplanar grains during crack growth [19]. Thus, the presence of ZrO_2 in the interdendritic zone deflected the main crack, rendering the fracture surface rougher compared to PM-NbZr1. The final fracture zone of the WAAM-NbZr1 also had comparatively more rough appearance than PM-NbZr1. This zone is mostly intergranular in the WAAM part, as seen in **Fig. 7**(h). Besides, the cracks formation path corresponds to the dendritic zone, with cracks primarily located in the interdendritic regions. On the other hand, in the PM-produced part shown in **Fig. 7**(d), a typical ductile failure mode with voids and cavities is evident. Fracture formation of WAAM-NbZr1 will be discussed in more detail in section 4.

3.5 Microstructure after fatigue

Fig. 8 displays the microstructure of WAAM and PM-NbZr1 after fatigue test. Most of the samples did not undergo any significant change in the sample except for the location close to fracture surface. In WAAM-NbZr1, the shear lip is more prominent compared to the fracture surface shown in **Fig.** 7. Deformation of the matrix is evident near the shear lip, where localized shear stress developed and the columnar dendrites are slanted toward the shear direction at an angle to the loading axis, as shown in **Fig.** 8(a). Voids are also evident at the interdendritic location where most of the ZrO_2 inclusions reside. Interestingly, the presence of fractured ZrO_2 particles was observed in the WAAM-NbZr1, as illustrated in **Fig.** 8(c). Inspections revealed that the fracture of these particles was predominantly influenced by their size and position within the microstructure. Specifically, particles exceeding a critical size threshold were more likely to rupture, primarily due to increased strain localization around them. This strain localization can be attributed to the larger surface area involved in the bonding between the particles and the surrounding matrix, which intensifies the stress concentration in these regions.

Furthermore, larger particles residing at the grain boundary triple points were also prone to fracture, as depicted in **Fig.** 8(d). This phenomenon can be explained by the grain boundary movement occurring in close proximity to the fracture zone during cyclic loading. The dynamic nature of these grain boundaries under repeated loading conditions may contribute to the weakening and subsequent rupture of particles located at these critical points. Apart from the triple points, oxide particles embedded within the grains themselves also exhibited similar deformation. Moreover, the formation of elongated voids was observed near these fractured particles as shown in **Fig.** 8 (h-j). These voids likely resulted from the same stress-state and cumulative strain conditions that contributed to particle fracture and debonding. The propensity for particle damage is significantly influenced by the stress-state and the accumulation of strain, which together determine the likelihood of particle fracture. In addition, the mismatch in elastic modulus and hardness between the particles and the surrounding grains plays a crucial role in localizing strain, further indicating potential sites for particle fracture [20]. The formation of voids in conjunction with particle fracture can be attributed to the stress triaxiality present at these specific locations within the microstructure. The appearance of these voids, along with their increasing size, suggests an ongoing process of damage accumulation throughout the specimen, which may ultimately contribute to the overall degradation of the material under cyclic loading conditions [21].

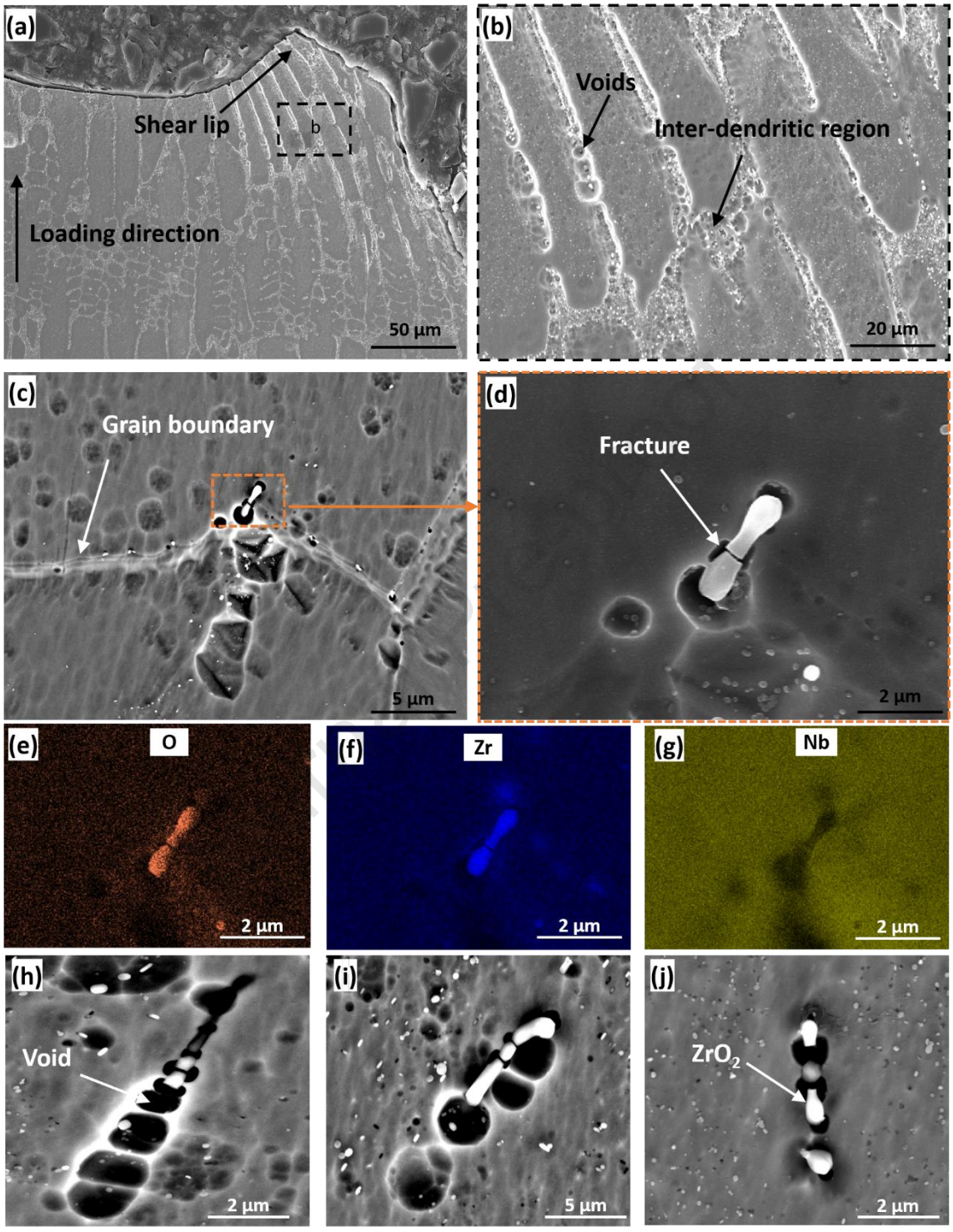

Figure 8: (a) Microstructure close to the fracture surface for WAAM-NbZr1, (b) magnified view of the black rectangle from indicating the deformation near the shear lip region, (c) fracture of ZrO_2 particle after fatigue test of stress level-1, (d) Microstructure near the fracture surface of PM-NbZr1, (e) magnified view from the red rectangle in (d) showing deformed matrix after fatigue test, (f) voids connecting parallel to the loading direction.

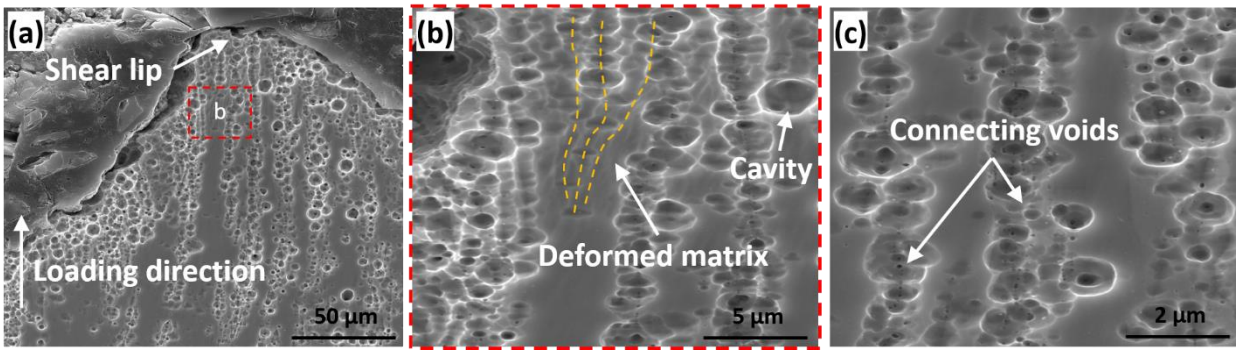

Figure 9: (a) PM-NbZr1 microstructure after fatigue test of SL-1. (b) Magnified version of the red rectangle from image (a) showing matrix deformation and (c) connecting voids near fracture surface.

In case of PM-NbZr1, the microstructure after fatigue test reveals a prominent shear lip as indicated in **Fig.** 9(a). Similar to the WAAM sample, the majority of the of the microstructure didn't undergo significant change during tensile fatigue loading. This also suggests that the fatigue cracks predominantly initiated from the surface irregularities of the sample rather than originating from within the microstructure. However, as we move closer to the fracture surface, some deformation within the matrix becomes evident. This matrix deformation can be identified by the alteration in the pre-exiting pore lines as shown in **Fig.** 9(b). Before the fatigue test, these porosities were primarily aligned with the rolling direction. However, as the material neared the end of its fatigue life, these lines became distorted at an angle relative to their original alignment. In addition to the deformation, connection of the pores to the loading direction is also clear as shown in **Fig.** 9(c).

4. Discussion

The effect of mean stress on fatigue life is particularly noticeable in stress-controlled cyclic loading or in the high-cycle fatigue region [22]. Strain accumulation increases with both stress amplitude and mean axial stress, which can further expedite the failure process in the presence of non-zero mean stress [23,24]. From experimental results in this study, similar effects were observed in the number of cycles at different stress levels. With constant stress ratio, an increase in mean stress led to a significant decrease in the number of cycles to failure, as depicted in **Fig.** 10. This is because tensile mean stress adversely affects fatigue life, resulting in a reduced useful life compared to compressive mean stress. Tensile stress promotes crack opening and accelerates the accumulation of fatigue damage.

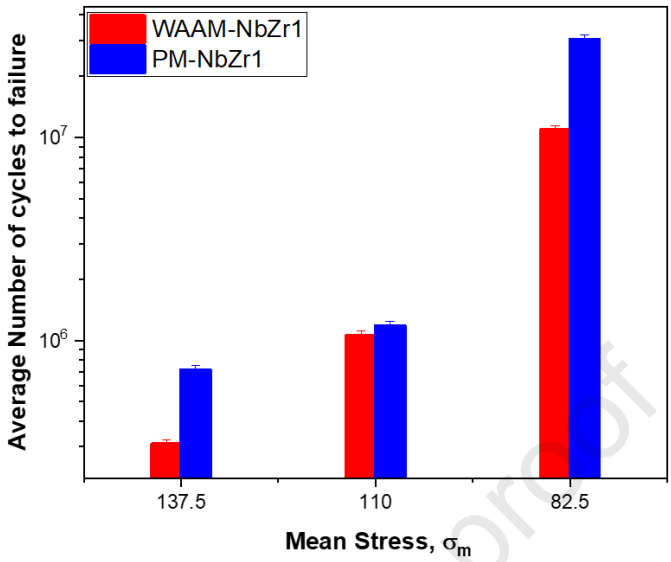

Figure 10: Mean stress vs average number of cycles to failure for PM-NbZr1 and WAAM-NbZr1.

Additionally, although both PM-NbZr1 and WAAM-NbZr1 samples demonstrated decreasing trend in the number of cycles to failure, all of the PM-NbZr1 samples had similar fracture surface morphology. On the other hand, for WAAM-NbZr1, the fracture surface displayed variations across different stress amplitudes. Specifically, the crack propagation region had the most significant dissimilarities, where the propagation criteria changed based on the applied maximum stress. **Fig.** 11(a-c) displays the crack propagation regions of the WAAM-NbZr1 for three different stress levels. In all of the cases, cleavage planes were identified in these regions, suggesting a transgranular type of crack propagation. The presence of cleavage planes also indicates reduced plastic flow in the WAAM-NbZr1 during propagation of cracks, which is typical for BCC metals like Nb [19]. Besides, damage accumulation is mostly based on void nucleation, growth, and coalescence-characteristic of the ductile failure mechanism-as evident in **Fig**. 7(f-h). This overlapping of ductile crack growth and cleavage planes in WAAM-NbZr1 underscores the heterogeneous nature of its dendritic microstructure.

For all the stress levels in WAAM-NbZr1, cleavage planes are primarily observed in the central region of the fracture surface, where crack propagation follows specific crystallographic planes under high stress. Concurrently, ductile crack growth occurred as voids nucleated, grew, and coalesced at the interdendritic zone around the ZrO_2 particles. This behavior reflects the interplay between brittle and ductile fracture mechanisms, as the crack path traverses regions with varying mechanical properties. Occasionally, ZrO_2 particles exhibit signs of fracture or decohesion from the matrix, as shown in Fig. 8(d), further emphasizing their role in the fracture process. This mixed-mode fracture mechanism arises from the brittle characteristics of ZrO_2 particles and the ductile nature of the Nb matrix, showcasing the complex interaction between these contrasting features. The crack growth pattern observed in WAAM-NbZr1 also exhibits a tunneling effect characteristic of ductile crack growth as evident from Fig. 12(a-c). The presence of shear lips, as illustrated in Fig. 8(a), further supports the tunneling effect during fracture for WAAM-NbZr1.

.

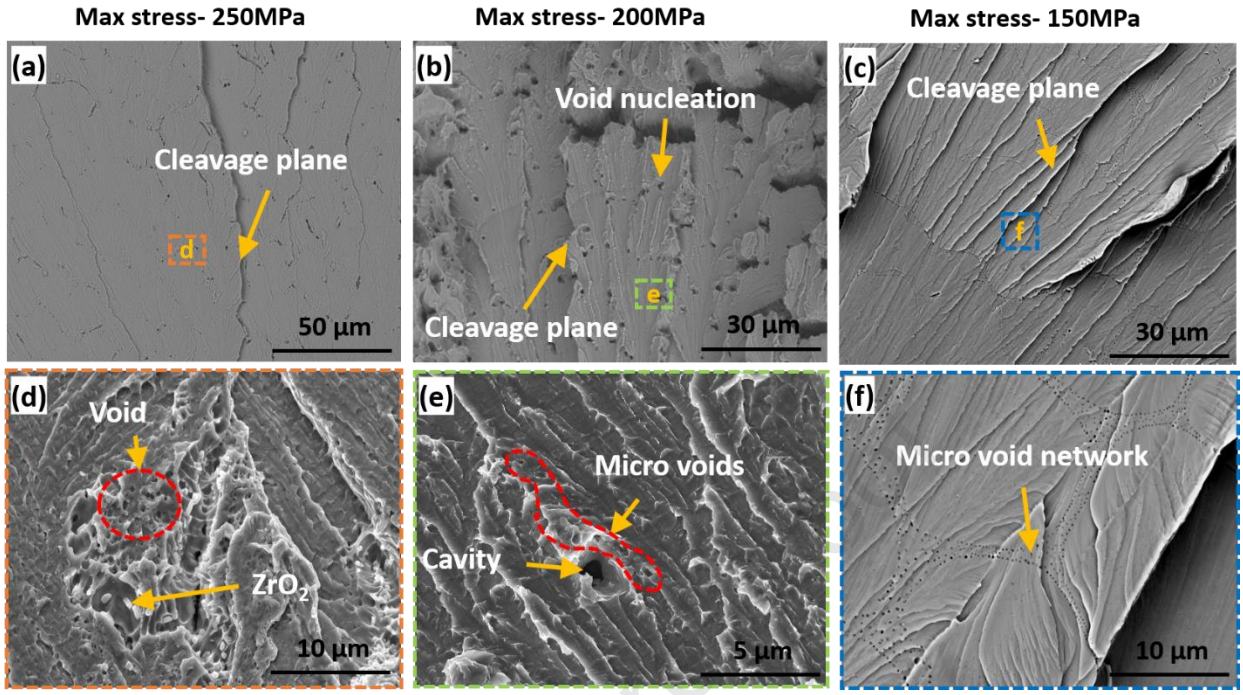

Figure 11: (a)-(c) Crack propagation zone from the fracture surface of WAAM-NbZr1 for three different stress levels, (d)-(f) enlarge view from (a)-(c) respectively.

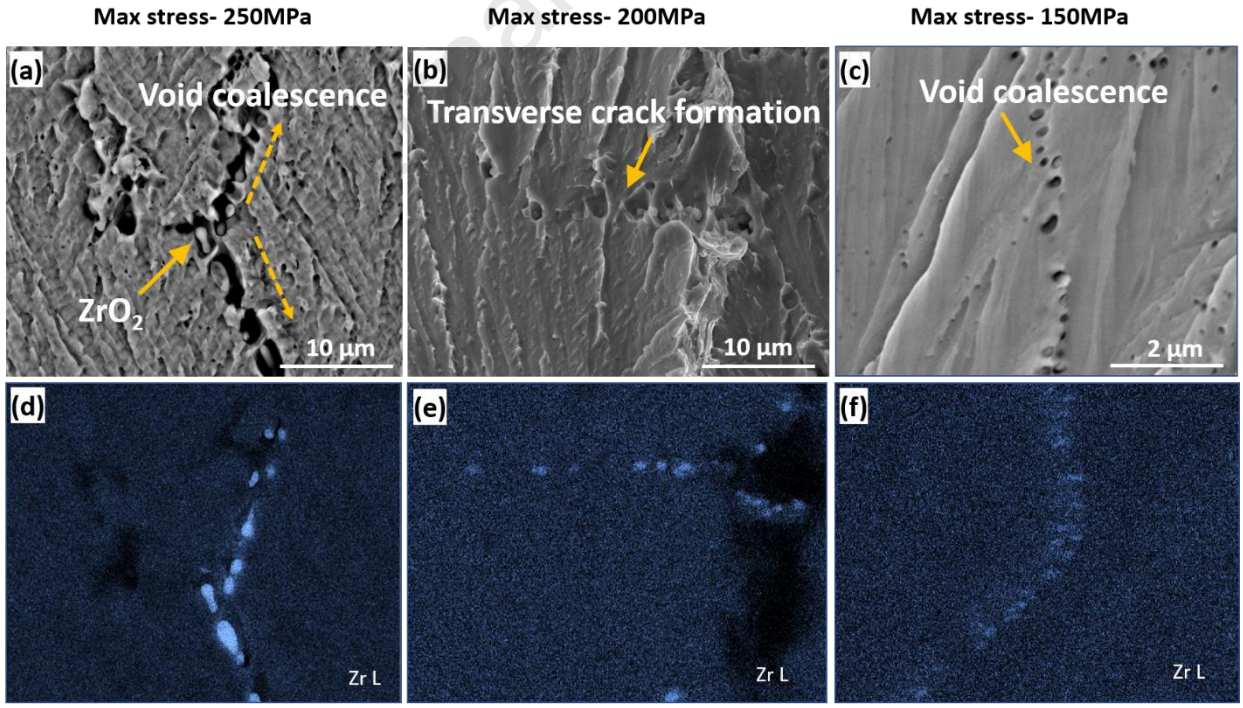

Figure 12: (a)-(c) Void coalescence location from the WAAM-NbZr1 fracture surface for three different stress level, (d)-(e) EDS spectra of Zr L showing the correlation of void location and ZrO_2 particles.

A noteworthy difference in the void size, their growth, and the way they are connected together with continued cyclic loading is observed in the propagation zone for WAAM-NbZr1 as evident from Fig. 11. During fracture, voids usually nucleate when sufficient stress is reached to break the matrix-particle interfacial bonding. The weaker binding force of the Nb matrix and secondary particle (ZrO_2) interfaces thus act as the priority site for void nucleation. For the highest peak stress (250 MPa), micro voids are observed to nucleate irregularly following the location of oxide particles. As plastic strains are not completely absent at the microscopic level, strain is mostly concentrated along the sheet of these voids, and with continued loading, local instabilities develop, leading to the void coalescence.

Furthermore, the location of micro-crack formation with connecting voids directs towards the presence of high stress-triaxiality for this loading condition ahead of the crack tip in the transverse direction. Consequently, voids are connected more readily, resulting in a combination of large transverse cracks and micro voids in the propagation zone. For a peak stress of 200 MPa, the void coalescence phenomenon is similar to stress level-1(peak stress-250MPa) as indicated in **Fig. 11**(b). Cavities are also present in the crack propagation zone around micro voids as shown in **Fig. 11**(e). Besides, from **Fig. 4**, it is evident that the difference between fatigue lives for these two loading conditions is very low. The rate of void growth and coalescence is significantly influenced by maximum and mean stress due to their effects on stress triaxiality, plastic deformation, and microstructural interactions. Higher stresses increase stress triaxiality, leading to localized strain concentration and reduced plastic deformation capacity, which accelerates void growth and coalescence. Additionally, higher stresses activate more void nucleation sites, particularly around hard inclusions like ZrO_2 particles, increasing void density and interaction. However, at the lowest peak stress of 150 MPa, the fatigue life is significantly enhanced. At this stress level, void coalescence occurred, leading to the formation of a micro void network distributed across the entire cleavage planes, as shown in **Fig. 11**(f). Based on the coalescence method, this sample demonstrated the most stable crack growth compared to other loading conditions. This can be explained by the fact that at lower stresses, plastic deformation is more evenly distributed, allowing strain hardening to delay void growth and coalescence. At higher stresses, crack tips remain sharp, enhancing void growth, whereas lower stresses promote crack tip blunting, which slows the process. Furthermore, in cyclic loading, higher mean stress results in greater residual stress, limiting recovery during unloading and speeding up void evolution, while lower mean stresses allow for more recovery and slower void growth.

The direction of void coalescence was primarily along the oxide particles in the interdendritic regions. EDS elemental mapping was conducted at selected locations on the fracture surface to identify the interdendritic region and correlate it with the connecting voids. **Fig. 12**(d-f) displays the Zr L spectra at the locations indicated in **Fig.12**(a-c). As seen from the mapping, the presence of ZrO_2 particles is vivid in these areas of preferred void coalescence.

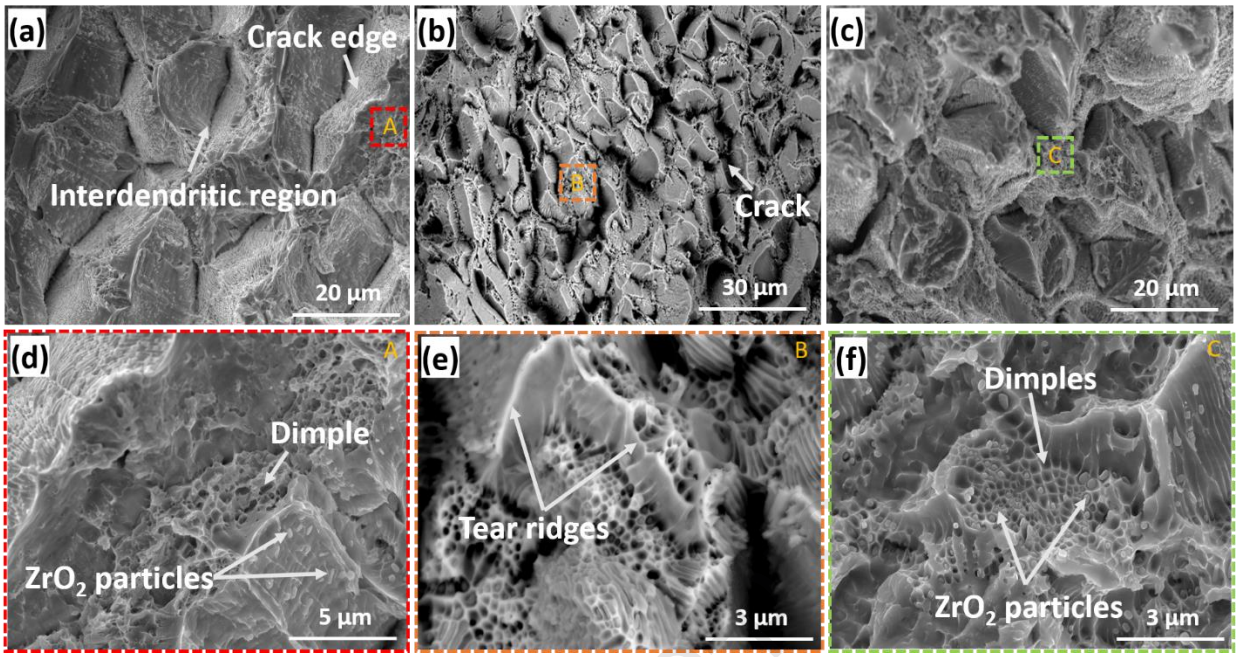

Figure 13: Final fracture area of WAAM-NbZr1 for stress level-1 (a,d), stress level-2 (b,e), and stress level-3 (c,f).

Despite variations in the void growth and connection mechanisms in the crack propagation area of WAAM-NbZr1 samples, the morphology of the final fracture areas remained largely consistent across all stress levels. **Fig. 13** shows the final fracture area of the WAAM-NbZr1 samples, which exhibit a fracture surface characteristic of intergranular failure. In these areas, the cracks are predominantly defined by the interdendritic regions, as illustrated in **Fig. 12**(a-c). During the propagation stage, cracks primarily advanced through the columnar grains while being intermittently stopped by the grain boundaries. Simultaneously, void growth and coalescence occurred under cycling loading, leading towards final ductile tearing in the interdendritic regions. The boundary of the dendrites is mostly occupied by ZrO_2 particles, as observed from fractography. Although the crack propagation zone, as seen in **Fig. 11**, is dominated by the void formation around the oxide particles, the final failure contains a mixture of voids and dimples in both dendritic and interdendritic regions (**Fig. 13**(d-f)). Tear ridges and dimples are also seen in the dendritic regions, which are primarily the Nb matrix, while cracks are mostly located in the interdendritic regions, accompanied by oxide particles.

Based on the above discussion, it can be anticipated that the inherent lower tensile strength values of the WAAM-NbZr1 had a substantial effect on its fatigue life when tensile-tensile cycling loading was applied. Besides, the interdendritic structures of the as-built WAAM-NbZr1, consisting of ZrO_2 particles, are identified as the most vulnerable areas. The presence of ZrO_2 is attributed to two major oxygen sources: (1) the significant oxygen content in the niobium wire, and (2) the atmospheric oxygen trapped in the melt pool during deposition. Consequently, reducing the oxygen level from both of these sources could reduce the amount of oxide inclusion in the WAAM-deposited NbZr1 thin walls. In high-cycle fatigue, the majority of the fatigue life is accounted for by the crack initiation stage. In high-cycle fatigue, most of the fatigue life is consumed during the crack initiation stage. Consequently, void nucleation sites play a crucial role in the initiation of fatigue cracks in WAAM-NbZr1. Therefore, controlling the location, size, and distribution of ZrO_2 particles is essential for enhancing the high-cycle fatigue life of WAAM-NbZr1. In addition, the

presence of residual stresses in WAAM-NbZr1 could also act as stress concentrators, generating new crack initiation sites. Consequently, minimizing residual stress would be highly beneficial in reducing the driving force for crack formation. Moreover, homogenization and aging heat treatment could be useful in improving the homogeneity and re-distribution of the ZrO_2 particles, reducing crack initiation sites and crack propagation rate [25]. This can also alleviate the directional properties of the columnar dendrite structure developed from the WAAM process, enhancing the tensile and fatigue strength of WAAM-NbZr1.

5. Conclusions

The tensile-tensile fatigue behavior of WAAM-produced NbZr1 alloy was investigated and compared to the performance of similar PM-produced alloys. On the basis of the experimental results obtained in this study, the major findings are listed below:

- WAAM-NbZr1 demonstrated lower resistance to fatigue failure compared to its PM counterpart in the tensile-tensile high-cycle fatigue region. The maximum number of cycles to failure was found to be $>10^7$ for PM-NbZr1, whereas WAAM-NbZr1 sustained around 10^7 cycles for a maximum tensile stress of 150 MPa.
- A large number of crack initiation sites were identified on the fracture surface of WAAM-NbZr1 compared to the PM-counterpart. Residual stresses in WAAM-NbZr1 might influence the generation of a substantial number of crack initiation sites. However, the presence of porosities did not have a significant effect on crack initiation in PM-NbZr1, as the pore sizes were very fine.
- The presence of ZrO_2 particles in the interdendritic regions significantly influenced the fatigue behavior of WAAM-NbZr1, playing a dominant role in void nucleation and coalescence. Crack propagation was mostly transgranular for WAAM-NbZr1, with simultaneous void nucleation following the oxide particles.
- The final failure was intergranular type for WAAM-NbZr1, and failure location resembled the shape of interdendritic regions. On the other hand, PM-NbZr1 exhibited typical ductile failure characteristics, including dimples and void coalescence.

Acknowledgement

Authors of this paper acknowledge the Center for Manufacturing Research (CMR) and Tennessee Technological University's Department of Manufacturing and Engineering Technology for their support. This material is based upon work supported by the National Science Foundation under Grant No. 2141905. This work was supported by the National Research Foundation of Korea (NRF) grant funded by the Korea government (MSIT) (No. RS-2024-00346883).

References:

[1] Gupta S, Jaypuria S, Pratihar D, Saha P. Experimental Investigation on Microstructure and Mechanical Properties of Laser-Welded Nb-1% Zr-0.1% C Alloy. J Mater Eng Perform 2021;30. https://doi.org/10.1007/s11665-021-05979-8.

[2] Paul W, S M. Fatigue of the alloy columbium (niobium) - one percent zirconium. MS Thesis Oregon State Univ 1964:59 pp.

[3] Begley RT, Platte WN, Lewis AI, Ammon RL. DEVELOPMENT OF NIOBIUM-BASE

ALLOYS. United States: 1961.

[4] Rubitschek F, Niendorf T, Karaman I, Maier HJ. Corrosion fatigue behavior of a biocompatible ultrafine-grained niobium alloy in simulated body fluid. J Mech Behav Biomed Mater 2012;5:181–92. https://doi.org/https://doi.org/10.1016/j.jmbbm.2011.08.023.

[5] Frazier WE. Metal Additive Manufacturing: A Review. J Mater Eng Perform 2014;23:1917–28. https://doi.org/10.1007/s11665-014-0958-z.

[6] Ahsan R, Tanvir ANM, Ross T, Elsawy A, Oh M-S, Kim DB. Fabrication of bimetallic additively manufactured structure (BAMS) of low carbon steel and 316L austenitic stainless steel with wire + arc additive manufacturing. Rapid Prototyp J 2019;ahead-of-p. https://doi.org/10.1108/RPJ-09-2018-0235.

[7] Islam S, Ahsan MRU, Seo G-J, Lee H-J, Park T, Pourboghrat F, et al. Investigations of Microstructure and Mechanical Properties in Wire + Arc Additively Manufactured Niobium–Zirconium Alloy. Adv Eng Mater 2023;n/a:2201633. https://doi.org/https://doi.org/10.1002/adem.202201633.

[8] Shah A, Aliyev R, Zeidler H, Krinke S. A Review of the Recent Developments and Challenges in Wire Arc Additive Manufacturing (WAAM) Process. J Manuf Mater Process 2023;7. https://doi.org/10.3390/jmmp7030097.

[9] Zahidin MR, Yusof F, Abdul Rashid SH, Mansor S, Raja S, Jamaludin MF, et al. Research challenges, quality control and monitoring strategy for Wire Arc Additive Manufacturing. J Mater Res Technol 2023;24:2769–94. https://doi.org/https://doi.org/10.1016/j.jmrt.2023.03.200.

[10] Marines I, Bin X, Bathias C. An understanding of very high cycle fatigue of metals. Int J Fatigue 2003;25:1101–7. https://doi.org/https://doi.org/10.1016/S0142-1123(03)00147-6.

[11] LUKÁŠ P, Kunz L. Specific features of high-cycle and ultra-high-cycle fatigue. Fatigue Fract Eng Mater Struct 2002;25:747–53. https://doi.org/10.1046/j.1460-2695.2002.00562.x.

[12] Calvo-García E, Valverde-Pérez S, Riveiro A, Álvarez D, Román M, Magdalena C, et al. An Experimental Analysis of the High-Cycle Fatigue Fracture of H13 Hot Forging Tool Steels. Materials (Basel) 2022;15. https://doi.org/10.3390/ma15217411.

[13] Milella PP. Fatigue and corrosion in metals. 2013. https://doi.org/10.1007/978-88-470-2336-9.

[14] Pradhan D, Mahobia GS, Chattopadhyay K, Fernando DC, Paulose N, Babu SNN, et al. Effect of stress ratio and mean stress on high cycle fatigue behavior of the superalloy IN718 at elevated temperatures. Mater Res Express 2019;6:0965a6. https://doi.org/10.1088/2053-1591/ab3321.

[15] Hauk VBT-S and RSA by NM, editor. Structural and Residual Stress Analysis by Nondestructive Methods, Amsterdam: Elsevier Science B.V.; 1997, p. iii. https://doi.org/https://doi.org/10.1016/B978-0-444-82476-9.50022-0.

[16] Avramovic-Cingara G, Saleh CAR, Jain MK, Wilkinson D. Void Nucleation and Growth in Dual-Phase Steel 600 during Uniaxial Tensile Testing. Metall Mater Trans A 2009;40:3117–27. https://doi.org/10.1007/s11661-009-0030-z.

[17] Yukitaka M, Masahiro E. Quantitative evaluation of fatigue strength of metals containing various small defects or cracks. Eng Fract Mech 1983;17:1–15. https://doi.org/https://doi.org/10.1016/0013-7944(83)90018-8.

[18] Dunstan MK, Paramore JD, Fang ZZ. The effects of microstructure and porosity on the competing fatigue failure mechanisms in powder metallurgy Ti-6Al-4V. Int J Fatigue 2018;116:584–91. https://doi.org/https://doi.org/10.1016/j.ijfatigue.2018.07.006.

[19] Janssen M, Zuidema J, Wanhill R. Fracture Mechanics: Fundamentals and Applications. 2004. https://doi.org/10.1201/9781482265583.

[20] HORSTEMEYER MF, YANG N, GALL K, McDOWELL D, FAN J, GULLETT P. High cycle fatigue mechanisms in a cast AM60B magnesium alloy. Fatigue Fract Eng Mater Struct 2002;25:1045–56. https://doi.org/https://doi.org/10.1046/j.1460-2695.2002.00594.x.

[21] Wisner B, Kontsos A. Investigation of particle fracture during fatigue of aluminum 2024. Int J Fatigue 2018;111:33–43. https://doi.org/https://doi.org/10.1016/j.ijfatigue.2018.02.001.

[22] Barbosa J, Correia J, Júnior RCS, De Jesus A. Fatigue life prediction of metallic materials considering mean stress effects by means of an artificial neural network. Int J Fatigue 2020;135:105527. https://doi.org/10.1016/j.ijfatigue.2020.105527.

[23] Vincent L, Le Roux J-C, Taheri S. On the high cycle fatigue behavior of a type 304L stainless steel at room temperature. Int J Fatigue 2012;38:84–91. https://doi.org/https://doi.org/10.1016/j.ijfatigue.2011.11.010.

[24] Maddox SJ. The effect of mean stress on fatigue crack propagation a literature review. Int J Fract 1975;11:389–408. https://doi.org/10.1007/BF00033527.

[25] Deirmina F, Davies PA, Casati R. Effects of Powder Atomization Route and Post-Processing Thermal Treatments on the Mechanical Properties and Fatigue Resistance of Additively Manufactured 18Ni300 Maraging Steel. Adv Eng Mater 2022;24:2101011. https://doi.org/https://doi.org/10.1002/adem.202101011.

Declaration of interests

☒ The authors declare that they have no known competing financial interests or personal relationships that could have appeared to influence the work reported in this paper.

☐The authors declare the following financial interests/personal relationships which may be considered as potential competing interests: